

Large-Eddy Simulation of Ship Flows with Wall-Layer Models on Cartesian Grids

Jianming Yang, Shanti Bhushan, Jung Soo Suh, Zhaoyuan Wang,
Bonguk Koo, Nobuaki Sakamoto, Tao Xing, and Frederick Stern
(IIHR-Hydroscience & Engineering, University of Iowa,
Iowa City, IA 52242, USA)

ABSTRACT

The recent development of CFDShip-Iowa Version 6, a high-performance, high-fidelity Cartesian grid solver for computational ship hydrodynamics, is presented. First, a wall function approach has been introduced for wall-layer modeling based on the immersed boundary method and the one-equation Spalart-Allmaras turbulence model. Second, in order to develop more advanced wall-layer modeling schemes, an orthogonal curvilinear grid solver based on the Cartesian grid solver has been implemented and tested. Third, a coupled level set volume-of-fluid method has been developed to substantially improve the volume conservation properties of the interface tracking/capturing schemes. In addition, fluid-structure interactions for ship motions in the framework of current Cartesian grid solver are also discussed. Finally, domain decomposition using MPI in all three directions has been included, parallel I/O becomes fully functional, and a new high-performance Poisson solver has been implemented. A series of cases ranging from the NACA0024 hydrofoil, Wigley hull, surface combatant DTMB model 5512, bow waves by a wedge, and surface-piercing circular cylinder, etc., have been carried out to validate the accuracy and demonstrate the scalability of the current method. Results including wave field patterns, velocity fields are successfully compared with experimental data and other computational results.

INTRODUCTION

Various Reynolds-averaged Navier-Stokes (RANS) solvers using body-fitted structured or unstructured grids have been developed and applied to ship hydrodynamics for the last two decades. Significant progress has been made with RANS solvers in terms of accuracy and capabilities (see, for example, Carrica et al., 2008 in this conference). However, hindered by the complicated mesh structures and

solution algorithms used in most RANS solvers, it is very difficult for them to run on grids of hundreds of millions of points and thousands of processors; and thus they can barely efficiently utilize the full potentials offered by the modern high performance computing systems.

As the petascale computing platforms emerge on the horizon, there has been noticeable endeavor recently to use large-eddy simulations (LES) and Cartesian grid methods in ship hydrodynamics applications. Among others, the Numerical Flow Analysis (NFA) code developed by Dommermuth et al. (see Dommermuth et al., 2007 and references therein) is one of major efforts on solving ship wave problems on Cartesian grids. In NFA, an immersed body method is used to model the ship geometry and a volume-of-fluid method is applied to capture the air/water interface. Simulations on grids with tens of millions of points and hundreds of processors have been demonstrated using NFA. However, the boundary layer is ignored in their simulations as a slip wall boundary condition applied to the ship hull. In Sussman (2005), a parallel, adaptive Cartesian grid approach was presented and an application in ship hydrodynamics was demonstrated. This method used a coupled level set/volume-of-fluid method for interface capturing and an embedded boundary method for the immersed geometries. The adaptive mesh refinement strategy can give much more flexibility on putting more grid points at interesting regions such as near-wall and air/water interface than a single block Cartesian grid. It can save a great deal of computational cost, although with a price of complicated solution algorithm. The velocity boundary conditions used at the ship hull were not discussed; thus it is not clear whether first- or second-order one-side discretization as in other Cartesian grid methods in the literature or slip wall condition was used. However, without some forms of wall-layer modeling methods, high-Re turbulent boundary layers common in ship flows can hardly be resolved even with local grid refinement due to the large number of

grid points required as discussed later. The CIP (Constrained Interpolation Profile) method is another Cartesian grid method that has been applied to ship wave problems. In Hu and Kashiwagi (2007), non-linear ship-wave interaction has been simulated using a CIP based method. The applicability of this method on large scale calculations and their treatments of wall-layer are unclear as only cases on small grids were shown.

At IIHR, CFDShip-Iowa Version 6, a parallel, high-fidelity Cartesian grid solver, has been developed for LES of turbulent two-phase flows in ship hydrodynamics. The objectives of this solver are the substantial improvements on scalability, speed, and accuracy over the previous versions, to be able to tackle multi-scale and multi-physics problems with billions of grid points and degrees of freedom on the oncoming petascale computers, and to provide turnkey capabilities for simulation-based design in ship hydrodynamics.

However, the application of Cartesian grid methods can become prohibitive for high Reynolds number flows due to the demanding resolution requirement near the wall boundary, since most of Cartesian grid methods approximate the velocity field near the wall boundary by a linear distribution, which is only correct in the viscous sublayer. For example, in order to resolve the viscous sublayer for a turbulent flow case at $Re = 10^6$, the near-wall grid spacing has to be within $2 \times 10^{-5}L$ (L is the reference length), and the total number of grid points will be more than a few billions. Therefore, some forms of wall-layer models have to be included such that the effects of boundary layer can be taken into account properly. Although the ultimate goal is to develop a hybrid grid method that uses unstructured grid to link the Cartesian background grid and body-fitted curvilinear grid for optimal efficiency, some studies on the performance of simple wall function approach with immersed boundary method on Cartesian grids and overset grid method using body-fitted orthogonal curvilinear grid and background Cartesian grid are necessary.

In this paper, wall-layer models and other issues have been addressed. Various tests have been carried out. Wall-layer modeling is performed using wall-functions approach. To achieve the objective multi-layer wall-function model is implemented using two-point approach for Spalart-Allmaras (1992) turbulence model. The model is validated for single-phase plate foil simulation, two-phase flow over NACA 0024 hydrofoil, and ship wave problems for Wigley hull and DTMB 5512 geometries. The two-phase flow past a surface-piercing circular cylinder has been simulated using LES on an orthogonal curvilinear grid. Detailed, volume-conserved bow wave breaking process by a deflecting plate in a flume has been compared with the

experimental data. Forced heave and roll motions of a square cylinder have been demonstrated. The DTMB 5512 case using a Cartesian grid with 268 million points on 1024 processors has been performed to showcase the scalability of the solver.

COMPUTATIONAL METHODS

The current study is based on the work in Yang & Stern (2008) and Yang et al. (2007), in which a level set based formulation for two-phase incompressible turbulent flows has been used and a sharp interface treatment (ghost fluid method) of the density at the air-water interface has been adopted. The level set evolution and reinitialization equations are solved using high-order schemes. A hybrid particle level set method is also developed as discussed in Wang et al. (2008a).

As the latest additions, a wall-layer modeling scheme based on wall function and one-equation Spalart-Allmaras turbulence model with the immersed boundary method on Cartesian grids has been developed in this study; a second-order PLIC volume-of-fluid method has been implemented and coupled with the level set method to provide volume-conserved interface tracking/capturing (Wang et al., 2008b); in addition, some preliminary studies of fluid-structure interactions in ship hydrodynamics field has been carried out. Other HPC additions such as domain decomposition in all three directions, parallel I/O based on MPI2, and a semi-coarsening multigrid Poisson solver using HYPRE library have also been completed.

Meanwhile, in order to investigate more advanced options for wall-layer modeling, an orthogonal curvilinear grid solver has been developed on the basis of the Cartesian grid solver. Note that the above-mentioned additions to the Cartesian grid solver haven't been converted to the orthogonal curvilinear coordinates yet, although their inclusions in the orthogonal curvilinear grid solver are planned.

For simplicity, vector notation will be used for all equations without regard to the coordinate systems in the following parts unless otherwise declared. The governing equations in indicial notation for orthogonal curvilinear coordinates are given in the Appendix.

Mathematical Modeling

Navier-Stokes Equations

The filtered Navier-Stokes equations are solved for the incompressible turbulent flows of two immiscible fluids, e.g., air and water:

$$\frac{\partial \bar{\mathbf{u}}}{\partial t} + \bar{\mathbf{u}} \cdot \nabla \bar{\mathbf{u}} = -\frac{1}{\rho} \nabla \bar{p} - \nabla \cdot \bar{\boldsymbol{\tau}} + \frac{1}{\rho} \nabla \cdot \bar{\mathbf{T}} + \mathbf{g}, \quad (1)$$

$$\nabla \cdot \bar{\mathbf{u}} = 0, \quad (2)$$

where \bar{f} denotes the filter operation on a variable f , t is the time, \mathbf{u} is the velocity vector, p is the pressure, ρ is the density, \mathbf{g} represents the gravity acceleration, and \mathbf{T} is the viscous stress tensor defined as

$$\mathbf{T} = 2\mu\mathbf{S}, \quad (3)$$

with μ the dynamic viscosity and \mathbf{S} the strain rate

$$\mathbf{S} = \frac{1}{2}(\nabla\mathbf{u} + (\nabla\mathbf{u})^T). \quad (4)$$

$\bar{\tau}$ is the subgrid-scale (SGS) and Reynolds stress tensor for LES and RANS as defined in the following part, respectively.

Turbulence Modeling

The deviatoric part of $\bar{\tau}$ in Eq. (1) can be parametrized following Smagorinsky's procedure for the LES approach and Boussinesq's hypothesis for the RANS approach respectively as follows:

$$\bar{\tau} - \frac{1}{3}\text{trace}(\bar{\tau})\mathbf{I} = -2\nu_T\bar{\mathbf{S}}, \quad (5)$$

although $\bar{\tau} = \overline{\mathbf{u}\mathbf{u}} - \overline{\mathbf{u}}\overline{\mathbf{u}}$ is the SGS stress tensor from the spatial filtering operation for LES and $\bar{\tau} = \overline{\mathbf{u}'\mathbf{u}'}$ is the Reynolds stress tensor from the Reynolds averaging (filtering) operation for RANS. Therefore, Eq. (1) can be rewritten in the following form

$$\frac{\partial\overline{\mathbf{u}}}{\partial t} + \overline{\mathbf{u}} \cdot \nabla\overline{\mathbf{u}} = -\frac{1}{\rho}\nabla\bar{p} + \nabla \cdot \left[\nu_T (\nabla\overline{\mathbf{u}} + (\nabla\overline{\mathbf{u}})^T) \right] + \frac{1}{\rho}\nabla \cdot \left[\mu (\nabla\overline{\mathbf{u}} + (\nabla\overline{\mathbf{u}})^T) \right] + \mathbf{g}, \quad (6)$$

with $1/3\text{trace}(\bar{\tau})$ incorporated into \bar{p} .

In LES, the turbulent eddy viscosity is defined as

$$\nu_T = C\Delta^2|\bar{\mathbf{S}}|, \quad \text{and} \quad |\bar{\mathbf{S}}| = \sqrt{2\bar{\mathbf{S}} \cdot \bar{\mathbf{S}}}. \quad (7)$$

The model parameter C in the eddy viscosity definition has to be determined to close the equations. In this paper the Lagrangian dynamic SGS model (Meneveau et al., 1996) is chosen as it can handle complex geometries without the requirement of homogeneous direction(s).

When a RANS or DES approach is used, the turbulent eddy viscosity is obtained by solving a transport equation for an auxiliary variable $\tilde{\nu}$ as proposed by Spalart and Allmaras (1992) (SA):

$$\frac{\partial\tilde{\nu}}{\partial t} + \mathbf{u} \cdot \nabla\tilde{\nu} = c_{b1}|\tilde{\Omega}|\tilde{\nu} - c_{w1}f_w\left(\frac{\tilde{\nu}}{\tilde{d}}\right)^2 + \frac{1}{\sigma}\left\{\nabla \cdot [(\mathbf{v} + \tilde{\nu})\nabla\tilde{\nu}] + c_{b2}|\nabla\tilde{\nu}|^2\right\} \quad (8)$$

The left hand side of the equation consists of the unsteady and advection terms of the turbulent eddy viscosity. The terms of right hand side are the production, destruction and diffusion, respectively. The turbulent eddy viscosity is obtained as:

$$\nu_T = f_{v1}\tilde{\nu} \quad (9)$$

where,

$$f_{v1} = \frac{\chi^3}{\chi^3 + c_{v1}^3}, \quad \chi = \frac{\tilde{\nu}}{\nu}. \quad (10)$$

The production term is based on the magnitude of vorticity:

$$|\tilde{\Omega}| = |\Omega| + \frac{\tilde{\nu}}{\kappa^2\tilde{d}^2}f_{v2}, \quad |\Omega| = \sqrt{2\Omega \cdot \Omega}, \quad (11)$$

$$\Omega = \frac{1}{2}(\nabla\mathbf{u} - (\nabla\mathbf{u})^T), \quad f_{v2} = 1 - \frac{\chi}{1 + \chi f_{v1}}$$

Mariani and Zilliac (1995) provided an improvement to the production term by suppressing the turbulence, i.e., excessive production of eddy viscosity in regions where vorticity magnitude exceeds the strain-rate.

$$|\tilde{\Omega}| = |\Omega| + f \min(0, |\mathbf{S}| - |\Omega|) + \frac{\tilde{\nu}}{\kappa^2\tilde{d}^2}f_{v2} \quad (12)$$

They conclude value of $f \sim 3.5-4.0$ provides best result for wingtip vortex calculations. In present calculations $f = 4.0$ is chosen. The destruction term involves a near-wall damping function which is:

$$f_w = g \left[\frac{1 + c_{w3}^6}{g^6 + c_{w3}^6} \right]^{1/6}, \quad (13)$$

$$g = r + c_{w2}(r^6 - r),$$

$$r = \frac{\tilde{\nu}}{|\tilde{\Omega}|\kappa^2\tilde{d}^2}$$

where \tilde{d} is the distance to the nearest wall in RANS approach.

In the DES approach, switch between RANS and LES is determined by setting $\tilde{d} = \min(d_{\text{RANS}}, d_{\text{LES}})$. In the RANS region length scale d_{RANS} is taken as the distance from the nearest wall whereas in the LES region the length scale is defines in terms of grid scale, $d_{\text{LES}} = C_{\text{DES}}\Delta$ with $\Delta = \max(\Delta x, \Delta y, \Delta z)$. The model constants are:

$$c_{b1} = 0.1355, \quad c_{b2} = 0.622,$$

$$c_{v1} = 7.1, \quad \sigma = 2/3,$$

$$c_{w1} = c_{b1}\kappa^{-2} + (1 + c_{b2})\sigma^{-1} = 3.239, \quad (14)$$

$$c_{w2} = 0.3, \quad c_{w3} = 2,$$

$$\kappa = 0.41, C_{\text{DES}} = 0.65$$

In the multi-phase flows the molecular eddy viscosity is smoothed across the interface using a Heaviside function (refer to Yang and Stern 2008) to avoid sharp gradients in molecular viscosity in Eq. (8).

In order to capture the effects of viscous boundary layers within the framework of a Cartesian grid solver, a multi-layer wall-function (WF) model capable of switching smoothly between sub-, buffer-, and log-layers (Bhushan et al. 2008) is used to specify velocity at the forcing points as:

$$\frac{U}{u_\tau} = \begin{cases} y^+ & : y^+ \leq 5 \\ \sum_{i=0}^4 a_i (y^+)^i & : 5 < y^+ \leq 30 \\ \kappa^{-1} \ln(y^+) + 5.1 & : y^+ > 30 \end{cases} \quad (15)$$

Subscripts F and P stand for the forcing and probe points, respectively, and $y^+_{F,P}$ is the normal distance between the F (or P) and immersed boundary in wall units. Model constants are:

$$\begin{aligned} a_0 &= -1.875736; \\ a_1 &= 1.8158144; \\ a_2 &= -0.102066044; \\ a_3 &= 0.00295224178; \\ a_4 &= -0.000033144178 \end{aligned} \quad (16)$$

The boundary condition for the SA model is specified as:

$$\tilde{v} = \kappa y^+ \text{Re} . \quad (17)$$

Interface Modeling

The position of the interface can be tracked as the zero level set of a signed distance function, ϕ , by solving the level set evolution equation

$$\frac{\partial \phi}{\partial t} + \mathbf{u} \cdot \nabla \phi = 0 . \quad (18)$$

To keep ϕ as a signed distance function in the course of the evolution, we iterate the reinitialization equation for the level set function as in Sussman et al. (1994)

In the coupled level set volume-of-fluid method, the volume-of-fluid function, F , is defined as the liquid volume fraction in a cell with its value in between zero and one in a surface cell and zero and one in air and liquid respectively. The advection equation of F is

$$\frac{\partial F}{\partial t} + \mathbf{u} \cdot \nabla F = 0 . \quad (19)$$

The fluid properties, such as density and viscosity, are defined using the level set function. The density retains its sharp jump across the interface, whereas the viscosity is smoothed over a transition region across the interface using a smoothed Heaviside function. The velocity across the interface is continuous, and the jump condition for stress is simplified as a smoothed viscosity is used. More details are presented in Yang and Stern (2008).

Rigid Body Motion

The rigid body motion of a elastically mounted body is modeled by a mass-spring-dashpot system as

$$\mathbf{M}\ddot{\mathbf{x}}(t) + \mathbf{C}\dot{\mathbf{x}}(t) + \mathbf{K}\mathbf{x}(t) = \mathbf{F}(t) \quad (20)$$

where \mathbf{M} is the mass matrix, and \mathbf{C} is the damping matrix, \mathbf{K} is the stiffness matrix, \mathbf{F} is the generalized force vector, $\mathbf{x}(t) = X_0(t)\mathbf{i} + Y_0(t)\mathbf{j} + Z_0(t)\mathbf{k}$ is the generalized displacement vector.

Numerical Method

Navier-Stokes Solver

The finite differences method is used to discretize the Navier-Stokes equations on a non-uniform staggered Cartesian grid, in which the velocity components u , v , and w are defined at centers of cell faces in the x , y , and z directions, respectively, and all other variables, i.e., p , ϕ , ρ , μ , and v_i are defined at cell centers. A semi-implicit time-advancement scheme is adopted to integrate the momentum equations with the second-order Crank-Nicolson scheme for the diagonal viscous terms and the second-order Adams-Bashforth scheme for the convective terms and other viscous terms. A four-step fractional-step method (Choi and Moin, 1994) is employed for velocity-pressure coupling, in which a pressure Poisson equation is solved to enforce the continuity equation. The convective terms are discretized using a third-order QUICK scheme (Leonard, 1979) and higher-order WENO schemes (Jiang and Shu, 1996) are available. All other terms are discretized with the standard second-order central difference scheme. Eq. (33) is approximated with the approximate factorization method (Beam and Warming, 1976) and the resulting tridiagonal linear equations are solved with the parallel tridiagonal system solver (Mattor et al., 1995). The parallelization is done via a domain decomposition technique using the MPI library. The pressure Poisson equation is solved using a multigrid-preconditioned Krylov subspace solver from the PETSc library (Balay et al., 2002). A new semi-coarsening multigrid Poisson solver from the HYPRE library from Lawrence Livermore National Laboratory (Falgout et al., 2006) has been added recently. In general, the Poisson solver is the most expensive part of the whole algorithm.

Wall Function Implementation

The wall-function is implemented using two-point approach following Gilmanov et al. (2003). It must be noted that V6 uses staggered grid, thus boundary condition for each velocity components is provided separately. The specific steps involved in the implementation of wall-function are as follows:

STEP 1: For every forcing point (F), the wall-normal distance (δ_n) and direction (\mathbf{n}) is obtained. Then a probe point (P) is identified along the wall-normal direction (\mathbf{n}) located at a distance $2\delta_n$ from immersed boundary. This ensures that the probe point is always surrounded by fluid points.

STEP 2: Velocity components are interpolated to P from the neighboring fluid points using tri-linear interpolation. The magnitude of the tangential (to the immersed body) velocity is then evaluated. The magnitude of the tangential velocity and wall distance of P is used in Eq. (15) to obtain friction velocity, u_τ . In

the buffer- and log-layers the equation are solved iteratively using Newton-Raphson method.

STEP 3: The friction velocity obtained in STEP 2 is then used in Eq. (15), to obtain the tangential velocity at F . The tangential velocity is mapped to the Cartesian direction to specify the velocities, e.g., U velocity is specified for U -forcing point similarly for other components.

STEP 4: To specify the boundary condition for turbulence model Eq. (17) is used, where the friction velocity is computed following STEPs 1-2.

STEP 5: Steps 1-4 are repeated every time step after the turbulence equation (Eq. 10) is solved.

In this paper, wall-function approach is used for calculation involving static bodies. However, for moving bodies special care has to be taken for the points inside the body which immerses into the fluids. Future work would involve development of the field extension approach used for near-wall solution for wall-function solutions.

Interface Tracking/Capturing

The level set and the reinitialization equations are solved using a third-order TVD Runge-Kutta scheme (Shu and Osher, 1988) for time advancement and the fifth-order HJ-WENO scheme (Jiang and Peng, 2000) for spatial discretization. The solution time of these equations does not pose a significant overhead as they are solved in a narrow band several grid-cells wide as detailed in Peng et al. (1999).

The coupled level set and volume-of-fluid (CLSVOF) method has been developed in order to improve the mass conservation property of the level set method. The interface is reconstructed via a PLIC scheme and the level set function is re-distanced based on the reconstructed interface. The interface is advected using a Lagrangian method with a second-order Runge-Kutta scheme for time integration. An efficient level set re-distance algorithm is explored, which significantly simplifies the complicated geometric procedure by finding the closest point on the reconstructed interface directly without considering the interface configuration in each computational cell. It is especially efficient for three-dimensional cases where various possibilities of the interface configuration exist. The performance of the CLSVOF method has been evaluated through the numerical benchmark tests and validation and application examples, where mass conservation has been well preserved. The details of this CLSVOF method are given in Wang et al. (2008a).

ODE Solver for Rigid Body Motion

Eq. (20) is coupled with Eqs. (1-2) since they provide fluid force (e.g. pressure and viscous forces) to the right hand side of Eq. (20). It can be rewritten in

non-dimensional form, as a system of $2n$ first-order, non-linear, ordinary differential equations where n is the number of degree of freedom of the body

$$\dot{\mathbf{z}}(t) = \mathbf{q}(t) \quad (21)$$

where

$$\mathbf{z} = [\tilde{\mathbf{x}} \quad \dot{\tilde{\mathbf{x}}}]^T, \mathbf{q} = [\dot{\tilde{\mathbf{x}}} \quad \tilde{\mathbf{F}}]^T \quad (22)$$

\mathbf{z} represents the generalized displacement and velocity vectors, and \mathbf{q} represents the generalized velocity and force vectors. There are two methods to couple the fluid solver with the equation of rigid-body motion. One method is so called weak-coupling where the fluid motion and rigid-body motion are solved alternatively. An explicit, 4th-order Adams-Bashforth scheme is adopted to predict the rigid-body motion of immersed bodies and an explicit Euler, two-step and three-step Adams-Bashforth methods are used for the first, second and third time step, respectively, to start the calculation. The other method is so-called strong-coupling where the fluid motion and rigid-body motion are solved simultaneously: this method is preferable than the weak-coupling method since the loads depend explicitly on \mathbf{z} and implicitly on the history of the motion and the acceleration of the body. Hamming's 4th-order predictor-corrector scheme is used to implement the strong-coupling method as described in Yang et al. (2008). In this method, the fluid and the structure are treated as elements of a single dynamical system, and all of the governing equations are integrated simultaneously and interactively in the time domain.

High Performance Computing

It is well-known that the simple topologic structure of Cartesian grids is extremely favorable for coarse-grain parallelization. A simple domain decomposition technique is used in CFDSHIP-Iowa V6 where the Cartesian grid is divided into uniform pieces, each of which resides in one processor. In Yang et al. (2007), only slab decomposition was used and the maximum number of processors could be used was determined by the number of grid points in one direction. In this study, domain decomposition in all three directions has been implemented, which facilitates the use of hundreds of processors even with coarse grids. All inter-processor communications for ghost cell information exchange have been changed into non-blocking mode. In general, optimal load balance can be achieved except for a small amount of overhead due to interface and immersed boundary treatment, which may be unevenly distributed over processors. Parallel I/O using MPI2 have been implemented such that all processors read from and write to one single file instantaneously, which is much more effective than one or a few processors receive data from all processors

and write to one or a few files and more convenient than every processor writes its own data files.

WALL-LAYER MODELING

Wall Function with Immersed Boundary

Plate Foil Simulation

Single-phase flow over a 2D plate foil is studied for low ($Re=3.33 \times 10^6$) and high Reynolds number ($Re=10^8$) flows. The thickness of the plate foil is 2% of the plate length and has a blunt leading edge (same geometry as Sanders et al., 2006 experiments). The computational domain is $2L \times L$ in streamwise and vertical directions, where L is length of the plate. V6-WF calculations are performed using $513 \times 257 \times 3$ and $610 \times 257 \times 3$ grid points for the low and high Re cases, respectively. The forcing points are mostly located in the range $y_F^+ \sim 30-100$. The body surface grid consists of 4K elements. Low Re results are compared with CFDSHIP-Iowa Version 4 (V4) (Carrica et al., 2007) near-wall ($250 \times 100 \times 5$ grid) and V4-WF ($200 \times 60 \times 5$ grid) solutions, and EFD data (Longo et al., 1998). High Re results are compared with V4-WF solution on $200 \times 75 \times 5$ grid, and EFD data of Sanders et al. (2006). In V4-WF simulations the grids were conveniently placed at $y^+ \sim 30$.

A fully developed turbulent boundary layer is expected on the plate surface; expect the blunt leading edge of the plate (Longo et al. 1998). It was observed that V6 near-wall results predicted larger recirculation region near the leading edge compared to V4 near-wall results. This could be due to the limitations of the SA model in predicting separated flows accurately (Wilcox, 2004), this aspect needs further investigation. Here results are compared only in the fully developed turbulent region away from the leading edge.

Skin friction variation along the plate foil is in good agreement with the V4 near-wall and V4-WF results, and within 3% of the EFD data for both low- and high Re cases. Results for high Re case is shown in Fig. 1(left). As shown in Fig. 1(center & right), good agreement is observed for the velocity and eddy viscosity profiles with the V4 results and analytic log-layer profiles. Overall, V6-WF provides good prediction of the turbulent boundary layer for Reynolds numbers equivalent to model-scale ship calculations.

NACA0024 Hydrofoil

Wave induced by a surface piercing NACA 0024 foil is simulated for the flow condition $Re=8.8 \times 10^5$ (water), $Fr=0.19$. Reynolds number for the air flow is $Re=5.9 \times 10^4$. This geometry has blunt bow and large beam and draft compared to a usual ship leading to relatively large bow wave and wide wake width. For this simulation condition, little or no separation is

observed in EFD, and the Kelvin wave system dominates. Half-domain simulation is performed assuming symmetry boundary condition on the center-plane. Computational domain is $8L \times 2L \times 3.24L$ in the streamwise, vertical, and spanwise directions, respectively, where L is the foil cord length. Two grids consisting of $256 \times 80 \times 64$ (coarse) and $256 \times 128 \times 80$ (fine) points with $y_F^+ \sim 200$ and 100, respectively, and a surface grid consists of 25K elements are considered. Results are compared with EFD data (Metcalf et al., 2006).

Attached streamlines are obtained both in air and water regions of the flow which proves that the flow is attached, which is consistent with EFD. Grid refinement shows significant improvement in the wave elevation pattern, when compared to EFD data. Fine grid result in Fig. 2 shows a prominent bow wave and subsequent trough followed by a series of transverse waves, which is in good agreement with the EFD data. Wavelength of the latter roughly corresponds to the theoretical value in a Kelvin wave pattern, i.e. $\lambda t = 2\pi Fr^2 \cong 0.23$.

The results demonstrate the ability of V6-WF to capture the Kelvin wave patterns. However, the Kelvin waves are displaced from the foil surface. This could be due to prediction of thicker boundary layer, compared to previous simulation using blended k-omega model (Kandasamy et al., 2005). Further improvements in the results are expected by using a finer grid.

Wigley Hull

Wigley hull with a steady forward speed advancing in calm water at $Re=2.2 \times 10^6$, $Fr=0.267$ is studied, the corresponding Reynolds number for the air-flow is $Re=1.47 \times 10^5$. Half domain ($3.5L \times 1.5L \times 2L$ in the streamwise, spanwise and vertical directions respectively) simulation is performed using $256 \times 68 \times 100$ (1.85 M) grid points with $y_F^+=150-200$. The simulation domain is extended to far-field both in air and water where slip-boundary conditions are used. Wigley hull surface grid consists of 13K elements. Results are compared with the CFDSHIP-Iowa-V.5 (V5) (Huang et al., 2007) near-wall half-domain solutions obtained on 332 K grid and EFD data (D'Este and Contento 2003). V6-Laminar solutions (Yang and Stern 2008) are also presented for comparison in the water region only.

Both V6-Laminar and V6-WF results predict the peak and amplitude of the Kelvin-waves in good agreement with the EFD, whereas, V5 results show a rapid diffusion of the Kelvin-waves. V6-WF performs better than V6-Laminar in predicting transom wave elevation pattern, when compared to EFD. Key results are presented in Fig. 3.

V6-WF predictions of the boundary-layer thickness are in good agreement with V5 results. This is a distinctive improvement over the V6-laminar results, where the boundary layer thickness is over-predicted. Representative plots at two streamwise locations ($x/L=0.5-0.8$) are shown in Fig. 4. As expected the boundary layer is thicker in the air region than the water region. However, V6-WF predicts thicker boundary layer in the air region compared to V5 results. The turbulent eddy viscosity obtained from V6-WF agrees well with V5 in the water region, but higher values are observed in the air region (Figure not shown). The difference could be either due to: (a) coarse grid in the air region, (b) coarse surface grid in the air region, or (c) differences in the turbulence model. Further investigation is required to understand the effect of grid resolution and/or turbulence modeling.

Model DTMB 5512

Flow around surface combatant model DTMB 5512 is performed at $Re=4.85 \times 10^6$ (water), $Fr=0.28$. The corresponding Reynolds number for the air flow is $Re=3.23 \times 10^5$. This geometry has a sonar dome, which provides an additional geometric complexity. The simulations are performed for the entire ship-hull on a domain extended to far-field in all the directions. Three different grid designs are considered: (a) Grid-1 computational domain is $4L \times 2L \times 2L$ resolved using $256 \times 128 \times 128$ (4.2M) grid points with $y_F^+ \sim 1000-1500$, and a coarse surface grid consisting of 7K elements. V6-WF and V6-Laminar simulations are performed on this grid to study the effect of turbulence modeling. (b) Grid-2 computational domain is $3.5L \times 1.5L \times 1.5L$ resolved using $256 \times 128 \times 128$ (4.2M) grid points with $y_F^+ \sim 400$, and a fine surface grid consisting of 40K elements. Simulations using V6-WF and V6-one way coupled RANS/LES (Yang and Stern, 2008) are performed on this grid. The latter simulation is performed by specifying the velocity at the forcing points obtained from V5 solution to demonstrate the applicability of wall-layer model. (c) Grid-3 computational domain is $4L \times 2L \times 2L$ resolved using $512 \times 256 \times 256$ (33M) grid points with $y_F^+ \sim 200$, and a surface grid consisting of 40K elements. Results are compared with V5-nearwall results obtained for half-ship domain on 615 K grid points. The EFD data used for validation is obtained from Longo et al. (2007).

Both V6-Laminar and V6-WF results on Grid-1 capture the Kelvin waves accurately but overpredicts the bow wave elevation compared to EFD data. V6-WF performs slightly better than V6-Laminar in depicting transom wave pattern, but elevation is significantly underestimated compared to EFD. V6-WF results on Grid-2 are in good agreement with the EFD data for the bow wave elevation pattern, and significant

improvement is observed in transom wave elevation. V6-WF results on Grid-3 shows further improvement in the transom wave elevation, however transom wave elevation is still under-predicted as seen in Fig. 5. V5-nearwall results show diffused Kelvin waves and over-predict the transom wave elevation.

Fig. 6 compares the streamwise velocity distribution on the nominal wake plane ($x/L=0.935$) with EFD data. V5-nearwall results underpredict the bulging of the boundary layer caused by the interaction between the sonar dome tip vortex and the boundary layer. V6-WF leads to better prediction of velocity contour shape compared to V6-Laminar solution on Grid-1, but boundary layer is much thicker compared to EFD. Results on Grid-2 show thinner boundary layer compared to Grid-1. V6-WF results on Grid-3 show further improve over the Grid 2 results. However, the roll-up of the velocity contour is not predicted, and the effect of sonar dome vortex is strong especially towards the center-plane. As expected, V6-Coupled RANS/LES shows good agreement in the boundary layer velocity distribution. But, the sonar dome vortex is not properly dissipated away from the hull. This is due to the lack of turbulent dissipation, as LES simulation does not receive any turbulence information from boundary layer.

Fig. 7 compares V6-WF turbulent boundary layer profiles with V5-nearwall solution. In V6-WF simulation, a stronger sonar dome vortex is observed, which interacts with the boundary layer throughout the hull. It is expected that probe points are located in the vortex region carrying low-momentum fluid, leading to underprediction of velocity and turbulent eddy viscosity in boundary layer. Significant improvement is expected if either finer grid is used, or a better turbulence model is considered which does not provide such strong vortex. The deck edge vortices are qualitatively similar in V6-WF and V5 simulations. As expected, deck edge vortices are predicted better when the finer surface grid is used.

Orthogonal Curvilinear Grid Solver

The Navier-Stokes solver and level set solver for orthogonal curvilinear coordinates have been validated using the fully developed turbulent channel flow at $Re_\tau = 180$ and a standard advection test Zalesak's disk, respectively. Other tests such as laminar ($Re = 270$) and turbulent ($Re = 2700$) single-phase flows past a circular cylinder have also been carried out to examine the code.

Here the turbulent two-phase validation test case compares LES predictions of a flow past a free surface piercing circular cylinder at Reynolds number $Re_D = 27,000$ and Froude number $Fr_D = 0.8$ (D is the diameter of the cylinder) with experimental data

obtained by Kawamura et al. (2002). The density ratio between air and water was set to 1/1000. A structured orthogonal grid consisting $130 \times 130 \times 130$ of points in the radial, circumferential, and vertical directions, respectively, is used. The outer boundary is divided into in- and outflow at $\theta = 90^\circ$ and $\theta = 270^\circ$, in which θ is the tangential angle starting from the downstream direction. Dirichlet boundary condition was used for the inflow boundary with uniform streamwise velocity $U_\infty = 1$ and convective boundary condition was used for outflow. A no-slip wall condition was enforced on the cylinder surface. Although the Reynolds number of the present flow is very high for LES (27,000), no special treatment was used to resolve near wall region. At the bottom (water side) and top (air side) of the computational domain, a slip wall boundary condition was used. Neumann condition (zero gradient condition) was applied at the whole boundary for the pressure and level set function. Since the in- and outflow direction is not aligned with the orthogonal grid system used in the present study, spurious wave reflection may be generated at the artificial boundary. In the present study, sponge layer suggested by Vogt and Larsson (1999) was used for three components of velocity and level set function. A circle with the radius of $20D$ was used for the computational domain and the width of sponge layer was set to $4D$ (about $2\pi Fr^2$ following Vogt and Larsson (1999)). The initial depths of air and water are set to $2D$ and $4D$, respectively.

Fig. 8 shows the time history and running mean of C_D ($F_D/(1/2\rho U_\infty^2 DH)$) and C_L ($F_L/(1/2\rho U_\infty^2 DH)$). Here $H = 4D$ (initial wet depth) was used to be consistent with Kawamura et al. (2002) although the present study computed both air and water flows. Both graphs show the flow is not converged to the statistically stationary state yet. The final mean C_D is 0.957, which is slightly smaller than 0.97 by the fine grid simulation by Kawamura et al. (2002). Strouhal number $St = fU_\infty/D$ from the C_L history is approximately 0.195, where f and U_∞ are the frequency of the lift coefficient and characteristic velocity (inlet velocity), respectively.

Fig. 9 shows the instantaneous evolution of air-water interface surface. Although the computed flow field is not fully developed yet, it shows a bow wave in front of the cylinder and Kelvin waves behind the cylinder. However, the length of recirculation region behind the cylinder is over-predicted and the depth of the region is also under-predicted due to the insufficient mesh resolution of immediately downstream of the cylinder. The maximum wall-unit distance (y^+) of adjacent cells to the cylinder is 14 and is a little high to resolve near-wall region accurately. One possible way to resolve this issue is the adoption of a wall function approach for the near wall region.

Since the Reynolds number of the present flow is very high ($Re = 27,000$), fully resolving the near wall region without any near-wall treatment requires huge computational resource and time. Hence wall function approach will improve the efficiency and accuracy of the present study.

To identify large-scale flow structures, an instantaneous iso-surface of the second invariant of the velocity gradient tensor $Q = 0.25$ is also shown in Fig. 9. Except the free surface, vortical structures in the vertical direction from the vortex shedding are observed. Relatively smaller structures are distributed near the cylinder and the sizes of the structures are increased as they are located away from the cylinder. Also, it is noted that the vortical structures in the air side are a lot bigger than the counterparts in the water side because Reynolds number of the air flow is about 10 times smaller than water flow. At the free surface, vortical structures are attached to the free surface and two-dimensional features by the vortex shedding are no longer observed.

Fig. 10 shows instantaneous vertical component of vorticity at different depths. At $z=-0.39$, the flow pattern is very similar to that for organized vortex-shedding an infinitely long cylinder. As the free surface is approached, smaller scale vortices are increased and the organized shedding of two large separated shear layers is significantly reduced. At the free surface, only vortices from shoulder wake and near-wake are observed. Kawamura et al. (2002) insisted the shear layers are inclined outward due to the deformation of the free surface so the formation of vortex shedding is no longer observed. Air flow region away from the free surface also shows that flow pattern becomes to organized structure and small scale vortices are disappeared (not shown).

Contour of the computed and measured mean surface elevation is shown in Fig. 11. Like Fig. 9, the hump on the upstream of the cylinder and the diverging Kelvin wave are clearly observed. However, the level depression computed in the present study is under-predicted and its length in streamwise direction is over-predicted, comparing with large eddy simulation and measurement by Kawamura et al. (2002). Fig. 11 shows the contour of the root-mean-square (r.m.s.) value of computed and measured fluctuation of the free surface. In the measurement by Kawamura et al. (2002), the peak value is located near the edge of the flat hollow part on the downstream side of the body. However, the present simulation predicted the peak locates the recirculation region immediately downstream of the cylinder. The over-estimated size of the recirculation region is responsible for the discrepancy.

The comparison between computation and measurement for the time-averaged elevation and r.m.s. fluctuation of the surface at two transverse sections on the downstream side of the cylinder is provided in Fig. 12. The present simulation failed to predict the depth of depressed hollow region and slope of the free surface at the edge of the hollow region. However, the mean elevation of free surface at the section $x=2.0$ is in reasonably good agreement with the experiment.

Comparison of mean streamwise velocity between measurement and computation is provided in Fig. 13. The decrease of streamwise velocity near the free surface is clearly seen. The prediction of existence of strong shear layer at the point $x=2.0$ and $y=1.0$ is consistent with Kawamura (2002).

BOW WAVE DYNAMICS

Ship bow waves exhibit both large and small scale features. The most prominent large scale feature is the Kelvin bow wave pattern scaled by Fr ; however, for sufficiently large Fr and depending on bow shape spilling and/or plunging breaking occurs inducing vortices and scars scaled by Re and We . Small Re and We inhibits breaking, i.e., in general model scale flows exhibit reduced breaking compared to full scale and smaller models display reduced breaking compared to larger models. Water quality scaling, e.g., fresh vs. salt water and surfactants are considered of secondary importance. A recent complementary EFD and CFD study has documented bow wave breaking and induced vortices and scars for 5415 for $Fr=0.35$ and capability CFDSHIP-Iowa Version 4 (Olivieri et al., 2007; Wilson et al., 2007). The most prominent small scale feature is the bow wave crest formation of thin overturning sheets which break up into spray. Re and We scale effects are large such that replication is difficult even with large models. The extent of the thin sheets is drastically reduced and remains attached, as shown by Stern et al. (1996) for the Series 60. However, studies for wedge flows by Waniewski et al. (2002) and Karion et al. (2004) display and document wave height and thin sheet formation, overturning jet thickness, fingering and spray, and plunging and splashing. These studies were selected as test cases for code development of CFDSHIP-Iowa Version 6 with regard to the capability of capturing small scale features in ship bow waves.

In Waniewski et al. (2002), typical bow wave profile obtained in the towing tank experiment shows a thin liquid sheet is created at the leading edge of the wedge, and it continues to ride up on the side wall. This thin liquid sheet starts to separate from the side wall as it reaches its maximum height. Once the crest reaches its maximum height, an overturning jet is formed and plunges back onto the undisturbed free

surface. A large area of splash is generated at the wake of the wedge due to wave plunge and air entrainment. In this study, the experimental data provided by Waniewski et al. (2002) will be used for the validation of the computational results.

The geometry of the wedge is similar to the large wedge model used by Waniewski et al. (2002). The side length of the wedge is $L = 0.75$ m, the height of the wedge is $H = 1.0$ m. The half wedge angle is $\theta = 26^\circ$ and the flare angle $\phi = 0^\circ$. In the case considered here, the water depth is $d = 0.0745$ m and the upstream velocity is $U = 2.5$ m/s, the corresponding Reynolds number, $Re = \rho U d / \mu$, is 1.64×10^5 , and the Froude number, $Fr = U / \sqrt{gd}$, is 2.93. The simulations are conducted on a computational domain of $x = [-1.0$ m, 6.0 m], $y = [-0.5$ m, 0.5 m] and $z = [0.0$ m, 3.0 m]. A non-uniform grid of 12.6 million points ($512 \times 96 \times 192$) with $\Delta h_{\min} = 0.003$ m is used. Uniform inflow and convective outflow boundary conditions are used. Slip wall boundary conditions are imposed at all the other boundaries.

Fig. 14 shows the computed bow wave profile which is compared with the experimental video image. As shown in the figure, the overall structure of the wave is similar to the experimental observations, such as the liquid sheet at the leading edge of the bow, overturning jet, jet plunging onto the free surface, and splash at the wake.

Surface disturbances were observed on the crest of the wave in the experiments (Waniewski et al., 2002). These surface disturbances appeared to be “finger-like” structures. Similar surface disturbances are also observed in the simulations as shown in Fig. 15. In the leading portion of the wedge, the liquid sheet is smooth. Surface disturbance starts at the middle portion and develops in the trailing portion.

A coarse grid of 9.4 million points ($384 \times 96 \times 256$) with minimum grid spacing $\Delta h_{\min} = 0.006$ m is also used in order to investigate the effect of the spatial resolutions on the wave elevation. The wave elevations along the side of the wedge for both coarse and fine grids are plotted in Fig. 16 with comparison to the experimental results. Although the wave profiles from both the CFD and experiment have the similar trend, the wave height is far below the experimental results. The wave elevation is significantly lower on the coarse grid than on the fine grid. The results computed on the fine grid are much closer to the experimental measurements. However, further grid refinement is still needed in order to match the experimental results.

Several possible reasons are likely accounting for the under-prediction of the wave elevation in the simulations. First, the grid resolutions are not enough to resolve the thin liquid sheet on the wall of the

wedge; the liquid sheet is thicker than the experimental results as can be seen from Fig. 15. Second, the boundary layer is not effectively resolved due to the lack of a turbulence model. Likely the velocity along the wedge side direction is over-predicted, whereas the velocity rising up in the vertical direction is under-predicted. Moreover, the contact angle is not properly considered in the simulations where the air/water interface is simply treated to be perpendicular to the solid wall. Wall adhesion effect due to the capillary force is not accurately implemented.

FORCED HEAVE/ROLL MOTIONS

In the first case, 2D square cylinder floating in the still water is subjected to prescribed heave motion in order to test the forces and moment calculation feature of the fluid solver. To prescribe the heave motion, vertical location of the centroid of the body is $y(t) = a/B\sin(\omega t)$ and relevant vertical velocity is $v(t) = a\omega/B\sin(\omega t)$. With $a/B = 0.2$ (a is the non-dimensional amplitude of oscillation, and B is the non-dimensional breadth of the cylinder), and $\omega = 1.0$ (non-dimensional), the results obtained are able to be compared with the previous computational results by Yeung and Anathakrishnan (1992). In addition to the prescribed heave motion, prescribed roll motion using the same geometry as the first case is also of interest and performed here. For this case, angular velocity is $\dot{\alpha}(t) = \alpha_0\omega\cos(\omega t)$ and acceleration is $\ddot{\alpha}(t) = -\alpha_0\omega^2\sin(\omega t)$ with $\alpha_0 = 0.1$ rad, $\omega = 6.4185$ rad/s. Different from the first case, the calculation is performed using dimensional values thus the output hydrodynamic moment is non-dimensionalized by

$$\bar{M} = \frac{4M}{\rho\alpha_0^2\omega^2B^2}$$

with ρ is the fluid density, and $B = 0.3048$ m is the dimensional breadth of the cylinder. The results are compared with the available experimental and computational results by Yeung et al. (1998).

Fig. 17 (upper left) presents the vorticity, and it is apparent that the sharp edge of the cylinder in water phase creates stronger vorticity. Fig. 17 (upper right) shows the vertical pressure force acting on the cylinder. Compared to the previous viscous flow computational result, the current result shows a good agreement in amplitude although the current result over-predicts the 1st harmonic by 5.5% compared to the reference result. About 10 degrees phase lag is observed at the peaks of minimum amplitude which is conjectured to be related to the added mass calculation.

Fig. 17 (lower left) presents the vorticity, showing that the vortices are shed from the sharp edge of the cylinder and is transported to upward/downward in water/air phase. Fig. 17 (lower right) shows the hydrodynamic moment acting on the cylinder.

Compared to the previous experimental and viscous flow computational results, the current result under-predicts the 1st harmonic by 23.2% compared to the experimental data and 11.9% compared to the viscous flow computational result with approximately 25° phase lead.

HIGH PERFORMANCE COMPUTING

In order to study the parallel computing performance of CFDSHIP-IOWA V6, extensive tests have been carried out for the ship model DTMB 5512 at $Fr = 0.41$. The computational domain for this case is $[-1,1] \times [-1,1] \times [-1,3]$ in the vertical, spanwise, and streamwise directions, respectively. The finest grid is $512 \times 512 \times 1024$, which gives a total number of 268.4 million grid points. The smallest grid spacing is about $0.0008L$ with L the ship length. The grid is non-uniform with refined zones around the bow and stern. A constant CFL number 0.6 is used and the time step is around $0.0002L/U$ with U the freestream velocity. But occasionally the time step can go down to $0.0001L/U$ due to strong localized wave breaking phenomena near the bow and in the wake.

The instantaneous air-water interface colored by the elevation is shown in Fig. 18. The breaking bow waves and scars induced by them are evident. The transom region is very energetic and a lot of wave breaking happens there. Fig. 19 shows the instantaneous vortical structures colored by streamwise vorticity. Interestingly, in the water phase, there are no large-scale structures shed from the sonar dome that usually can be found in RANS/DES calculations; although these small-scale structures are still attracted to and interact with the ship hull after about a distance of one third ship length. The near-hull structures are then conveyed downstream and reach the stern, where they interact and mix with the complex transom vortical structures. It is remarkable that two vortical filaments induced by bow waves on each side of ship hull retain their sizes and strength and extend into the far wake where the grid becomes very coarse. For the instantaneous vortical structures in the air phase, the most distinct structures are the two leading edge vortices which extend into the far wake. Their interactions with the transom air flow induce some helix vortices around each leading edge vortex. Some vortical structures generated by breaking bow waves are also visible along the air/water interface.

Three coarser grids, $256 \times 256 \times 512$, $128 \times 128 \times 512$, and $64 \times 64 \times 258$, obtained by taking every second, fourth, and eighth point from the finest grid, respectively, are used in the scalability study. Fig. 20 shows the weak/strong scalability of CFDSHIP-IOWA V6. Two cases are given in the figure for weak scalability test: 262,144 grid points per processor with

2, 16, 128, 1024 processors and 524,288 grid points per processor with 1, 8, 64, 512 processors. In theory, a weak scaling factor of one should be expected as each processor handles the same amount of data. However, the CPU time for the Poisson solver on a finer grid increases due to the Poisson solver in this study is a semi-coarsening multigrid solver from the HYPRE library, in which the semi-coarsening process is performed down to a $1 \times 1 \times 1$ grid. It is evident extra levels of coarsening have to be used for finer grids, which produces extra computational cost.

The strong scalability of CFDSHIP-Iowa V6 is carefully examined. Due to the conflict between the available memory and the problem size, only the $128 \times 128 \times 512$ can finish a full curve from 1 to 1024 processors (maximum available resource in this study). For this grid, ideal speedup can be obtained with 2 and 4 processors. Then the performance falls below optimal as the number of processors increases and a speedup of 16 is shown with 32 processors. This case is still scalable up to 128 processors and after that no gain or even penalty can be seen with more processors. For grid $256 \times 256 \times 512$, ideal speedup is shown when the number of processors increasing from 8 (not able to run on less than 8) to 16. This case is scalable up to 256 processors. For the finest grid $512 \times 512 \times 1024$, no ideal speedup is demonstrated as this case cannot be run on less than 128 processors. Nevertheless, the solver is proven to be scalable up to 1024 processors. It is reasonable to expect it will be scalable with more processors. Tests will be performed when resources are available.

CONCLUSIONS AND FUTURE WORK

Recent development on several aspects of CFDSHIP-Iowa V6 is presented. Wall-layer modeling with immersed boundary method is achieved by implementing a multi-layer wall function model for SA turbulence model. The model is first validated using turbulent boundary layer flow over a plate foil and Kelvin waves induced by a surface piercing NACA0024 hydrofoil. Then it is further validated for ship-flows using Wigley hull and DTMB 5512 geometries. It is observed that Kelvin wave pattern is not significantly affected by the turbulence modeling, but boundary layer and transom wave elevations are predicted better in WF simulations. Results also show strong dependence on grid resolution. Overall, present results are encouraging and demonstrate the potential of using wall function approach as a viable option for wall-layer modeling for immersed boundary methods. As the first step towards more advanced wall-layer models, an orthogonal curvilinear grid solver for LES of two-phase turbulent flows is developed based on the Cartesian grid solver. A LES of the flow past a free-surface piercing circular cylinder is simulated for

validation of the solver. Important features of free surface such as bow waves in front of the cylinder and Kelvin wakes are matched with the experimental data well on a relative coarse grid. To investigate the performance of CLSVOF in the Cartesian grid solver on realistic wave breaking problem, the bow wave dynamics by a wedge is simulated. The overall bow wave profile, plunging jet shape, and surface disturbances on the wave crest are similar to the experimental observations. Some preliminary results on forced heave/roll motions of a square cylinder are also presented to demonstrate the idea of simulating 6DoF ship motion with V6. As discussed in the previous parts, LES of ship flows on Cartesian grids requires high resolution grids and the capability of running on grids of billion points and thousands of processors is crucial for V6. Significant improvements have been made in terms of HPC aspects of V6 and a series of tests have been carried out to demonstrate the scalability of V6 on grids of hundreds of thousands of points and thousands of processors.

There are several issues that need to be addressed in the near future for wall-layer modeling. Present calculations using V6-WF predicts stronger vortices than V5 results. This could be due to the limitations of SA model. As discussed by Wilcox (1993), SA model has deficiencies in predicting jet-like free-shear regions and separated flows, e.g., separation bubble is overpredicted by as much as 60% in backward facing step. Kim and Rhee (2002) reported that SA model fails to predict roll-up of the vortex sheet, wake width and wake fraction accurately for flow around KVLCC hull. On the other hand, blended $k-\varepsilon/k-\omega$ model have been successfully used for ship flows in V4 and V5, which will be implemented to eliminate uncertainties surrounding turbulence modeling issues.

In addition, in order to predict ship motions on Cartesian grids using immersed boundary methods, the forces and moments calculation must be implemented for 3D geometries. When the forces and moments are available, the next step, the implementation of weak/strong coupling scheme between fluid solver and structure solver as in Yang et al. (2008), becomes straightforward. One option is to introduce non-inertial reference coordinate system (for instance, Kim and Choi, 2006) so that the calculation of one arbitrary moving body will be very efficient as the immersed boundary setup step is done only once and which is an expensive operation when a very fine surface grid for the 3D geometry is used.

It is evident that the current Cartesian grid solver with wall function approach for immersed boundary methods can be an accurate and simple-to-use tool for ship hydrodynamics. However, very expensive grid density is required to resolve the immersed boundary, e.g., 33M grids used for 5512 geometry leads to

$y^+ \sim 200$. It must be noted that best results using WF are obtained when $y^+ \sim 100$ (Bhushan et al. 2008), which is hardly achieved using Cartesian grids with tens of millions of points. Body fitted curvilinear grid are most suitable for conveniently placing the grid point. Thus next step is to couple the Cartesian grid solver and the orthogonal curvilinear grid solver when the latter has all the components, such as turbulence models, wall functions, and VOF, from the former. The orthogonal curvilinear grid solver can be used as a replacement of the current wall function approach for immersed boundary methods by only solving the turbulent boundary layer equations or RANS momentum equations. Of course, overset grid methods can also be used as in V4 to obtained fully coupled solutions. Although the ultimate goal is a hybrid grid method with an unstructured grid solver to link the body-fitted curvilinear grids and the background Cartesian grids, the overset grid approach can also be a valuable way to investigate and explore various numerical methods.

Furthermore, it is no doubt that the CLSVOF method can be used to significantly improve the volume conservation properties of the level set method and capture more small-scale interfacial phenomena as shown in the results. However, it also deteriorates the strict time step constraint imposed by the explicit treatment of convective terms. In the current CLSVOF method, a geometrical Lagrangian advection scheme is used to calculate VOF fluxes and not convenient to be treated implicitly. Therefore, an alternative approach will be the semi-Lagrangian schemes for the advection terms to avoid the stringent time step limitation without sacrificing the overall second-order accuracy of the spatial discretization. Other options such as local time stepping and fully implicit schemes will also be explored to investigate pros and cons.

To further improve the efficiency and applicability of the current solver, multi-block structured grids and local refinement techniques will be implemented. With some forms of deferred correction for curvilinear grid non-orthogonality, the current Cartesian grid solver and orthogonal curvilinear grid solver can be combined to produce an efficient multi-block structured grid solver that can handle most ship hydrodynamics applications with ease. The local refinement techniques for structured grids are mature to some extent and can be implemented within a relatively short time frame. These techniques are especially advantageous for immersed boundary methods as refined grid blocks can be arranged on places near the immersed interfaces and large amount of grid points can be saved with regard to a single block grid.

Other improvements in usability such as boundary conditions specification and user interface will be implemented along with the above development to provide a high-performance, high-fidelity, user-

friendly tool for ship hydrodynamics simulation-based design.

APPENDIX: GOVERNING EQUATIONS ON ORTHOGONAL CURVILINEAR GRIDS

The derivation and notation for the curvilinear orthogonal coordinate by Pope (1978) are adopted.

Continuity Equation

$$\nabla(i)[u_i] = 0$$

where u_i is the velocity in orthogonal coordinate ξ_i direction and $\nabla(i) = \frac{1}{J} \frac{\partial}{\partial \xi_i} \left(\frac{J}{h_i} \right)$. Also, J is Jacobian of coordinate transformation, and $h_i = \frac{\partial x_i}{\partial \xi_i}$, here x_i is a Cartesian coordinate. Jacobian J and h_i are related as follows:

$$J = h_i h_j h_k.$$

Momentum Equation

$$\frac{\partial u_i}{\partial t} + \nabla(j)[u_i u_j] - \frac{1}{\rho} \nabla(j)[\tau_{ij}] = -\frac{1}{\rho} \frac{\partial p}{\partial \xi(i)} + H_j(i) \left[u_j u_j - \frac{\tau_{ij}}{\rho} \right] - H_i(j) \left[u_i u_j - \frac{\tau_{ij}}{\rho} \right] + g_i$$

where ρ is the density, p is the pressure, t is the time, and g_i is the gravity vector in the ξ_i direction. Also, $H_i(j) = \frac{1}{h_i h_j} \frac{\partial h_i}{\partial \xi_j}$ and $\partial \xi(i) = h_i \partial \xi_i$.

Also, viscous stress tensor τ_{ij} is defined as follows:

$$\tau_{ij} = (\mu + \nu_t \cdot \rho) S_{ij}$$

where μ is the dynamic viscosity and ν_t is the eddy viscosity. S_{ij} is the strain rate

$$S_{ij} = \frac{\partial u_i}{\partial \xi(j)} + \frac{\partial u_j}{\partial \xi(i)} - u_i H_i(j) - u_j H_j(i) + 2u_i H_i(l) \delta_{ij}.$$

Level Set Equation

Air-water interface is tracked by solving the level set equation

$$\frac{\partial \phi}{\partial t} + \frac{u_i \partial \phi}{\partial \xi(i)} = 0.$$

ACKNOWLEDGMENTS

This research was sponsored by the Office of Naval Research under Grant N00014-01-1-0073 and N00014-06-1-0420, under the administration of Dr. Patrick Purtell.

REFERENCES

- Balay, S., Buschelman, K., Gropp, W., Kaushik, D., Knepley, M., Curfman, L., Smith, B. and Zhang, H. "PETSc User Manual", ANL-95/11-Revision 2.1.5, 2002, Argonne National Laboratory.
- Beam, R.M. and Warming, R.F., "An implicit finite-difference algorithm for hyperbolic systems in conservation-law form", *J. Comput. Phys.*, Vol. 22, 1976, pp. 87-110.

- Bhushan, S., Xing, T., Carrica, P. and Stern, F. "Model-and full-scale URANS simulations of Athena resistance, powering and seakeeping, and 5415 maneuvering", J. Ship Res., 2008, submitted.
- Carrica, P.M., Wilson, R.V., and Stern, F., "An unsteady single-phase level set method for viscous free surface flows", Int. J. Num. Meth. Fluids, Vol. 53(2), 2007, pp. 229-256.
- Carrica, P.M., Huang, J., Noack, R., Kaushik, D., Smith, B., and Stern, F., "Toward large-scale computations of ship motions with dynamic overset curvilinear grids", Proc. 27th Symp. Naval Hydrodynamics, 2008, Seoul, Korea.
- Choi, H. and Moin, P., "Effects of the computational time step on numerical solutions of turbulent flow", J. Comput. Phys., Vol. 113, 1994, pp. 1-4.
- D'Este, F. and Contento, G., "Time domain linear and weakly nonlinear coupled wave resistance and seakeeping computations", Science & Supercomputing at CINECA, Report, 2003.
- D. G. Dommermuth, T. T. O'Shea, D. C. Wyatt, T. Ratcliffe, G. D. Weymouth, K. L. Hendrikson, D. K. P. Yue, M. Sussman, P. Adams and M. Valenciano, "An Application of Cartesian-Grid and Volume-of-Fluid Methods to Numerical Ship Hydrodynamics", Proc. 9th Inter. Conf. Numer. Ship Hydrodynamics, 2007, Ann Arbor, Michigan.
- Falgout, R.D., Jones, J.E., and Yang, U.M., "The design and implementation of HYPRE, a library of parallel high performance preconditioners", in Numerical Solution of Partial Differential Equations on Parallel Computers, A.M. Bruaset and A. Tveito, eds., Springer-Verlag, **51** (2006), pp. 267-294.
- Gilmanov, A., Sotiropoulos, F., and Balaras, E., "A general reconstruction algorithm for simulating flows with complex 3d immersed boundaries on Cartesian grids", J. Comput. Phys., Vol. 191, 2003, pp. 660-669.
- Hu, C. and Kashiwagi, M., "Numerical and experimental studies on three-dimensional water on deck with a modified Wigley model", Proc. 9th Inter. Conf. Numer. Ship Hydrodynamics, Ann Arbor, Michigan, 2007.
- Huang, J., Carrica, P. M. and Stern, F. "Coupled ghost fluid/two-phase level set method for curvilinear body fitted grids", Int. J. Num. Meth. Fluids, Vol.55, 2007, pp. 867-897.
- Jiang, G.-S. and Peng, D., "Weighted ENO schemes for Hamilton-Jacobi equations", SIAM J. Sci. Comp., Vol. 21, 2000, pp. 2126-2143.
- Jiang, G.-S. and Shu, C.-W., "Efficient implementation of weighted ENO schemes", J. Comput. Phys., Vol. 126, 1996, pp. 202-228.
- Kandasamy, M., "URANS for unsteady free-surface wave-induced boundary layer separation", Ph.D. thesis, The University of Iowa, 2005.
- Karion, A., Fu, T. C., Sur, T.W., Rice, J.R., Walker, D.C. and Furey, D.A., "Experiment to examine the effect of scale on a breaking bow wave", Carderock Division, Naval Surface Warfare Center, Hydromechanics Research and Development report, 2004, NSWCCD-50-TR-2004/060.
- Kawamura, T., Mayer S., Garapon, A. and Sorenson, L., "Large eddy simulation of a flow past a free surface piercing circular cylinder", J. Fluids Eng., Vol. 124, 2002, pp.91-101.
- Kim D. and Choi H. "Immersed boundary method for flow around an arbitrary moving body", J. Comput. Phys., 2006;212:pp. 662-680.
- Kim, S. E., and Rhee, S. H., "assessment of eight turbulence models for a three-dimensional boundary layer involving crossflow and streamwise vortices", 40th Aerospace Sciences Meeting & Exhibit, AIAA 2002-0852, Reno, NV.
- B.P.Leonard, "A stable and accurate modelling procedure based on quadratic interpolation", Comput. Methods Appl. Mech. Engrg., Vol. 19, 1979, pp. 58-98
- Longo, J., Huang, H.P., and Stern, F., "Solid-fluid juncture boundary layer and wake", Experiments in Fluids, Vol. 25(4), 1998, pp. 283-297.
- Longo, J., Shao, J., Irvine, M., and Stern, F., "Phase-averaged PIV for the nominal wake of a surface ship in regular head waves", J. Fluids Eng., Vol.129, 2007, pp.524-540.
- Mariani-D, J., Zilliac, G. G., Chow, J. S. and Bradshaw, P., "Numerical/experimental study of a wingtip vortex in the near field", AIAA J., Vol. 33(9), 1995, pp. 1561-1568.
- Mattor, N., Williams, T.J., and Hewett, D.W., "Algorithm for solving tridiagonal matrix problems in parallel," Parallel Comput., Vol. 21, 1995, pp. 1769-1782.
- Meneveau, C., Lund, C.S., and Cabot, W.H., "A Lagrangian dynamic subgrid-scale model of turbulence," J. Fluid Mech., Vol. 319, 1996, pp. 353-385.
- Menter, F. R., "Two-equation eddy viscosity turbulence models for engineering applications", AIAA J., Vol.32, 1994, pp.1598-1605.
- Metcalf, B., Longo, J., Ghosh, S., Stern, F., "Unsteady free-surface wave-induced boundary-layer separation for a surface-piercing NACA 0024 foil: towing tank experiments", J. Fluids Struct., Vol. 22, 2006, pp. 77-98.
- Olivieri, A., Pistani, F., Wilson, R., Campana, E., and Stern, F., "Scars and vortices induced by ship bow wave breaking", J. Fluids Eng., Vol. 129, 2007, pp. 1445-1459.
- Peng, D., Merriman, B., Osher, S., Zhao, H., and Kang, M., "A PDE-based fast local level set method", J. Comput. Phys., Vol. 155, 1999, pp. 410-438.

Pope, S. B., "The calculation of turbulent recirculating flows in general orthogonal coordinates", *J. Comput. Phys.*, Vol. 26, 1978, pp. 197-217.

Sanders, W. C., Winkel, E. S., Dowling, D. R., Perlin, M., and Ceccio, S. L., "Bubble friction drag reduction in a high-Reynolds-number flat-plate turbulent boundary layer", *J. Fluid Mech.*, Vol. 552, 2006, pp. 353-380.

Shu, C. W. and Osher, S., "Efficient implementation of essentially non-oscillatory shock-capturing schemes," *J. Comp. Phys.*, Vol. 77, 1988, pp. 439-471.

Spalart, P. R. and Allmaras, S. R., "A one-equation turbulence model for aerodynamic flows", AIAA Paper 92-0439, 1992.

Stern, F., Longo, J., Zhang, Z.J., and A.K. Subramani, "Detailed bow-flow data and CFD of a Series 60 CB = .6 ship model for Froude number .316", *J. Ship Res.*, Vol. 40, 1996, pp. 193-199.

Sussman, M., "A parallelized, adaptive algorithm for multiphase flows in general geometries," *Comp. Struct.*, Vol. 83, 2005, pp. 435-444.

Sussman, M., Smereka, P. and Osher, S., "A level set approach for computing solutions to incompressible two-phase flow," *J. Comp. Phys.*, Vol. 114, 1994, pp. 146-159.

Vogt, M and Larsson, L., "Level set methods for predicting viscous free surface flows", Proc. 7th Int. Conf. on Numerical Ship Hydrodynamics, 1999, Nante, France

Wang, Z., Yang, J., Koo, B., and Stern, F., "A coupled level set and volume-of-fluid method for sharp interface simulation of plunging breaking waves", *Inter. J. Multiphase Flow*, under review, 2008a.

Wang, Z., Yang, J., and Stern, F., "An improved particle correction procedure for particle level set method", *J. Comput. Phys.*, under review, 2008b.

Waniewski, T.A., Brennen, C.E. and Raichlen, F., "Bow wave dynamics," *J. Ship Res.*, Vol. 46, 2002, pp. 1-15.

Wilcox, D.C. (2004), *Turbulence Modeling for CFD*, 2nd Ed., DCW Industries, Inc.

Wilson, R., Carrica, P. and Stern, F., "Simulation of ship breaking bow waves and induced vortices and

scars", *Int. J. Num. Meth. Fluids*, Vol. 54, 2007, pp. 419-451.

Yang, J., and Stern, F., "Sharp interface immersed-boundary/level-set method for wave-body interactions", *J. Comput. Phys.*, under review, 2008.

Yang, J., Sakamoto, N., Wang, Z., Carrica, P.M. and Stern, F., "Two phase level-set/immersed-boundary Cartesian grid method for ship hydrodynamics", Proc. 9th Inter. Conf. Numer. Ship Hydrodynamics, Ann Arbor, Michigan, 2007.

Yang, J., Preidikman, S., and Balaras, E., "A strongly-coupled, embedded-boundary method for fluid-structure interactions of elastically mounted rigid bodies", *J. Fluids Struct.*, Vol. 24, 2008, pp. 167-182.

Yeung R.W. and Ananthakrishnan P., "Oscillation of a floating body in a viscous fluid", *J. Eng. Math.*, Vol. 26, 1992, pp. 211-230.

Yeung R.W., Liao S.W. and Roddier D., "On roll hydrodynamics of rectangular cylinders", Proc. 8th Inter. Offshores Polar Eng. Conf., 1998, Montreal, Canada.

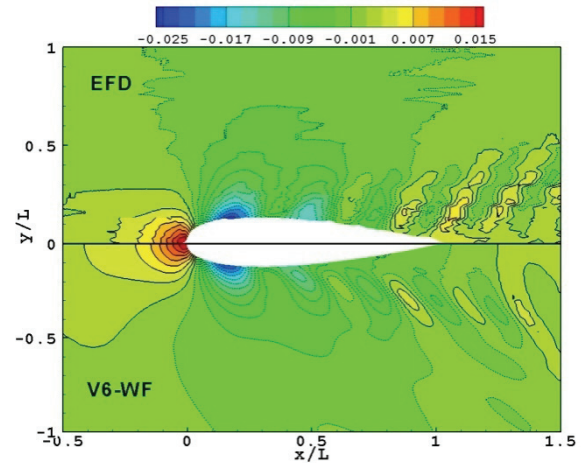


Fig. 2: Contours of wave elevation for NACA 0024 at $Fr = 0.19$ obtained from V6-WF on fine grid is compared with EFD data (Metcalf et al., 2006).

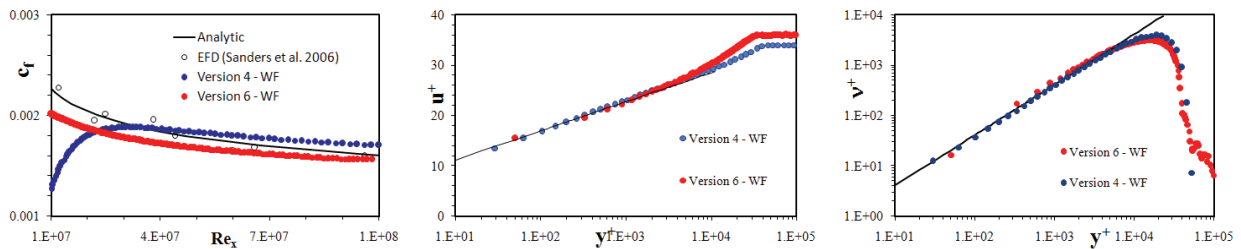


Fig. 1: Turbulent boundary layer over a plate foil. Left: Skin friction coefficient along the plate foil compared with EFD data (Sanders et al., 2006); Center: Streamwise velocity; Right: Eddy viscosity profiles compared with log-law analytic profile at $Re_x = 8 \times 10^7$. Analytic profiles are: $c_f = 0.0263 \times Re_x^{-1/7}$, $u^+ = \frac{1}{\kappa} \ln(y^+) + 5.1$, $\nu_T^+ = \nu_T/\nu = \kappa y^+$, respectively.

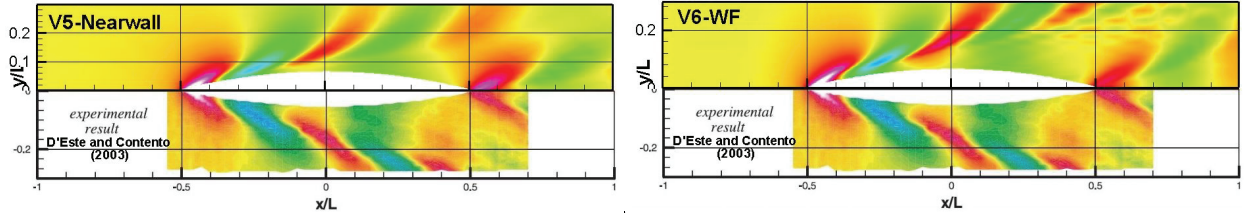


Fig. 3: Wave elevation profile for Wigley hull at $Fr = 0.267$ compared with EFD data (D'Este and Contento, 2003). Left: V5-nearwall; Right: V6-WF. Contours from -1.2×10^{-2} to 1.2×10^{-2} with intervals of 2.4×10^{-3} .

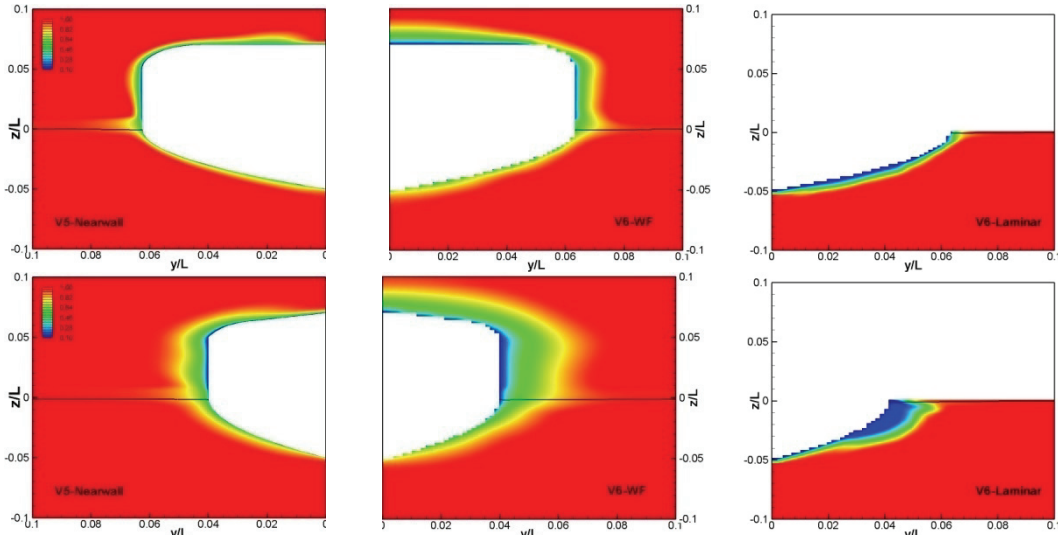


Fig. 4: Streamwise velocity contours at two streamwise locations. Top: $x/L = 0.5$; Bottom: $x/L = 0.8$. are compared for V5-nearwall (left), V6-WF (center), and V6-Laminar (right) results for Wigley hull ($Fr = 0.267$).

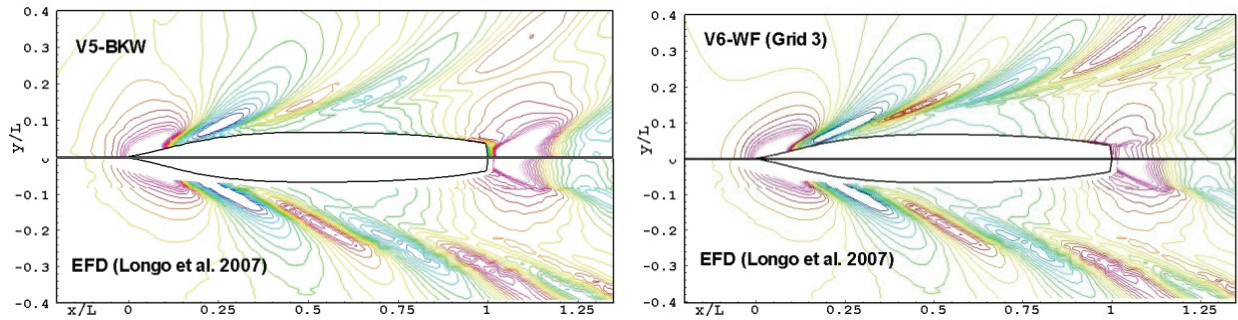


Fig. 5: Instantaneous wave field obtained from V5-nearwall (left) and V6-WF (right) solutions on Grid 3 are compared with EFD data for DTMB 5512 ($Fr = 0.28$). Contours from -5×10^{-3} to 5×10^{-3} with intervals of 5×10^{-4} .

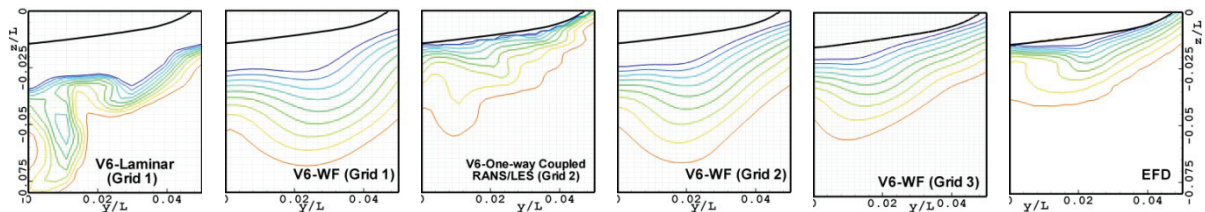


Fig. 6: Comparison of the streamwise velocity distribution on the nominal wake plane ($x/L=0.935$) for DTMB 5512 ($Fr = 0.28$). V6-Laminar on Grid 1, V6-WF on Grid 1, V6-One-way coupled RANS/LES on Grid 2, V6-WF on Grid 2, V6-WF on Grid 3 are compared with EFD data (Longo et al. 2007) (grids are shown as overlay). Contours are from 0.55 to 0.95 with intervals of 0.05.

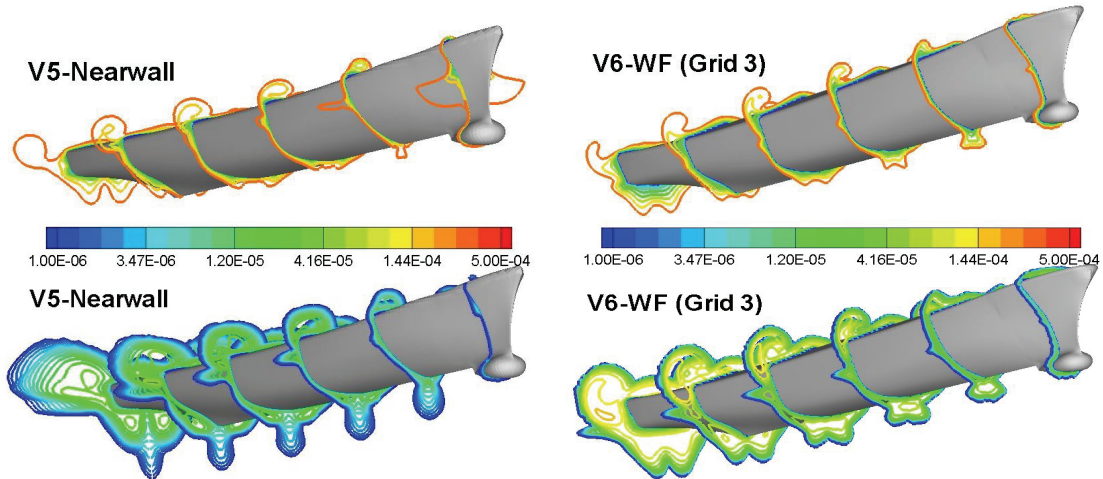


Fig. 7: V5-nearwall and V6-WF on Grid 3 are compared for streamwise velocity (top), and turbulent eddy viscosity (bottom) contours on several streamwise locations ($x/L = 0.05 \sim 1.0$) for DTMB 5512 ($Fr = 0.28$). Velocity contours are from 0.1 to 1.0 with intervals of 0.1.

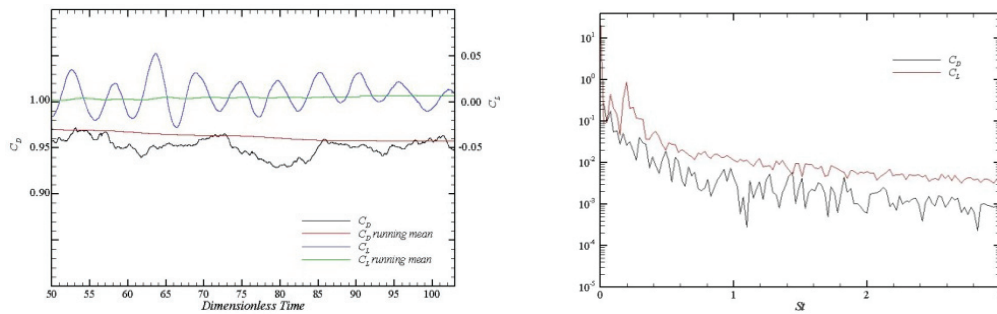


Fig. 8. Time history, running mean and FFT of drag and lift coefficients. Left: Time history, running mean; Right: FFT (log scale).

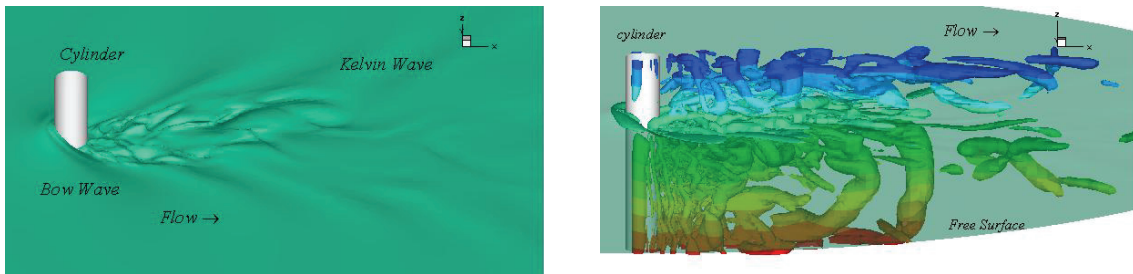


Fig. 9. Two-phase flow past a surface-piercing cylinder. Left: Instantaneous air-water interface; Right: instantaneous vortical structures colored by pressure, $Q = 0.25$.

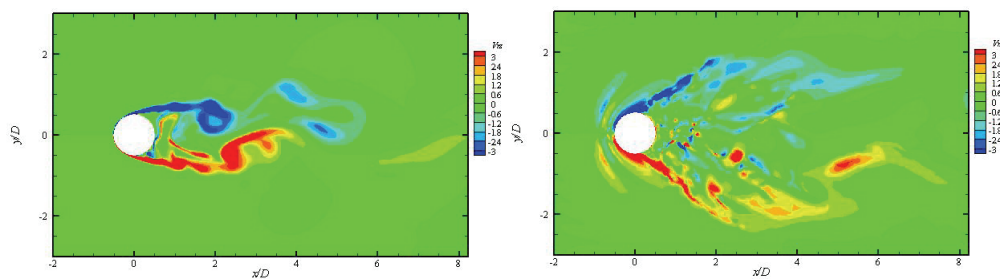


Fig. 10. Comparison of the instantaneous vertical vorticity component on horizontal planes. Left: $z = -3.9$; Right: air-water interface.

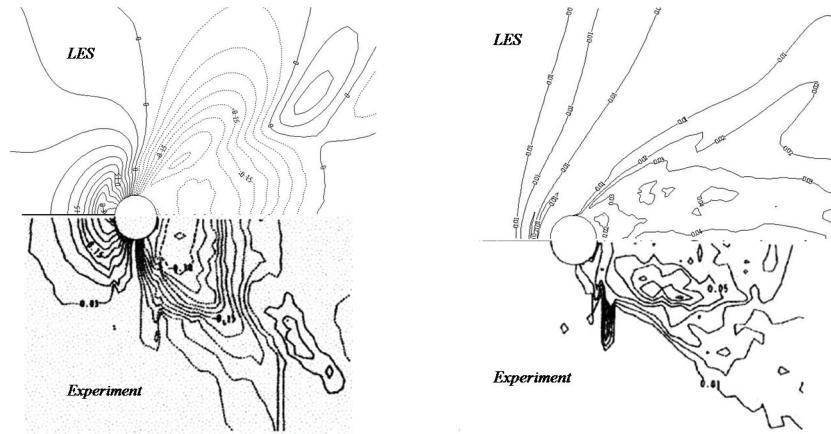


Fig. 11. Computed and measured (Kawamura, 2002) mean surface elevation (Left) and r.m.s. of the interface fluctuation (Right) around a surface-piercing cylinder.

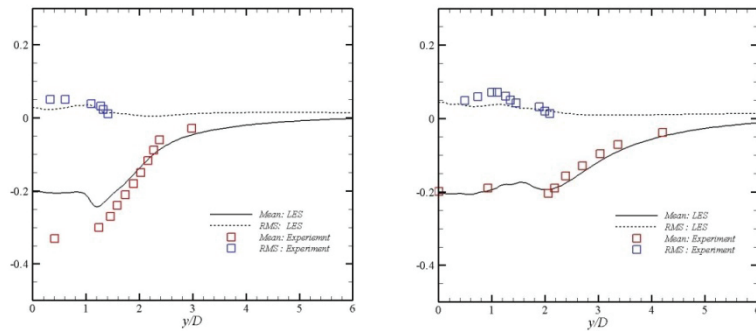


Fig. 12. Profiles of the time-averaged elevation and r.m.s. fluctuation of the free surface. Left: $x = 0.9$; Right: $x = 2.0$.

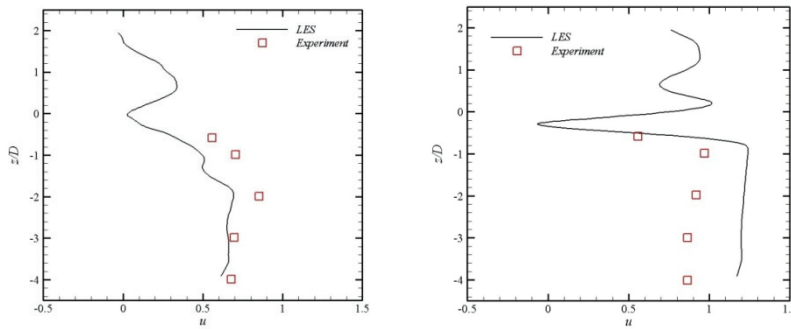


Fig. 13. The vertical profile of the computed and measured mean streamwise velocity. Left: $x = 4.5, y = 0$; Right: $x = 2, y = 1$

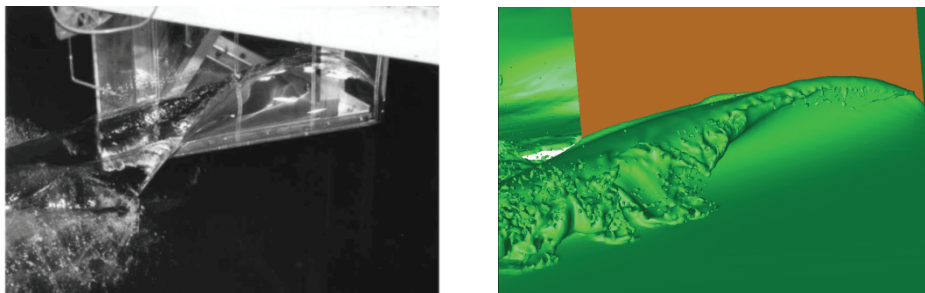


Fig. 14. Bow wave profile, $Fr = 2.93$. Left: experiment (Waniewski et. al, 2002); Right: simulation.

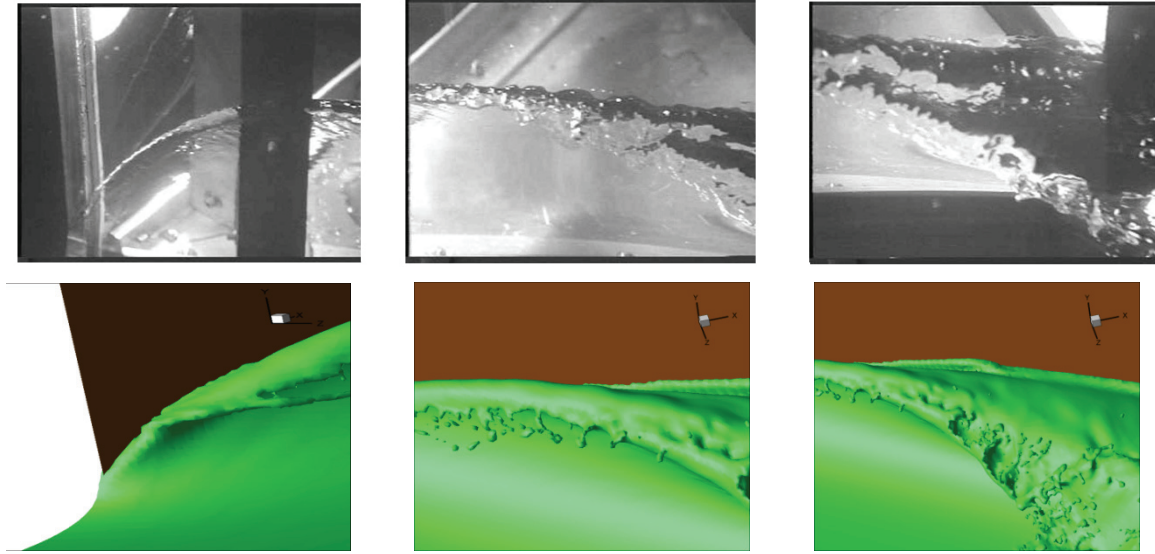


Fig. 15. Free surface disturbance on the wave crest, $Fr = 2.93$. Top: experiment (Waniewski et. al, 2002); Bottom: simulations. Left: leading portion; Center: middle portion; Right: trailing portion.

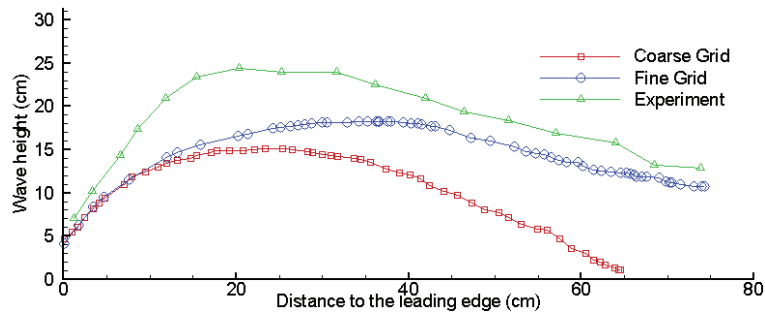


Fig. 16. Comparison of the wave profile with the experimental results, $Fr = 2.93$.

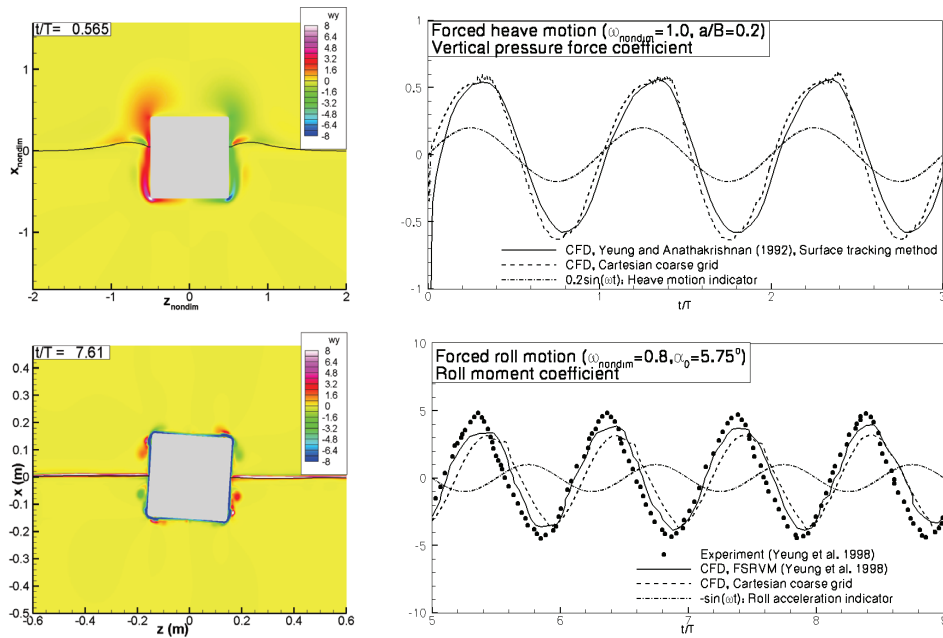


Fig. 17. Forced heave/roll square cylinder. Left: free surface and vorticity contours; Right: comparison of force/moment with reference data.

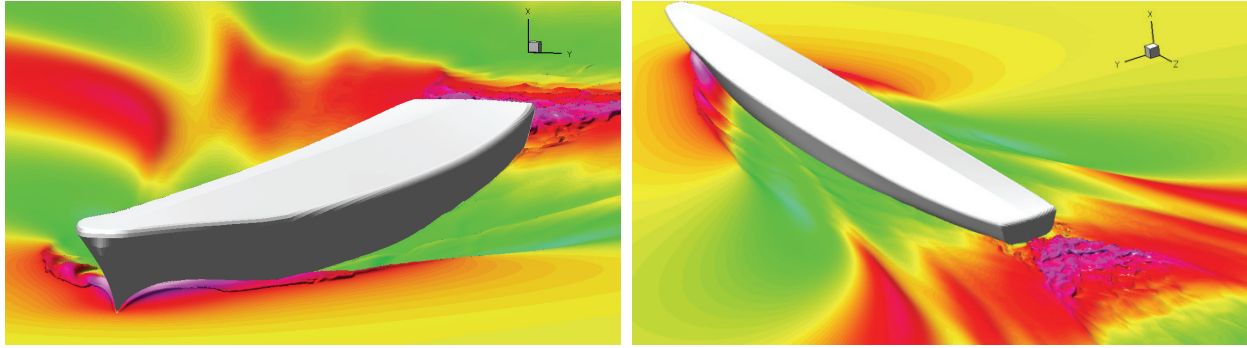


Fig. 18. Instantaneous air/water interface colored by elevation for DTMB 5512 at $Fr = 0.41$. Left: Bow waves; Right: Transom waves.

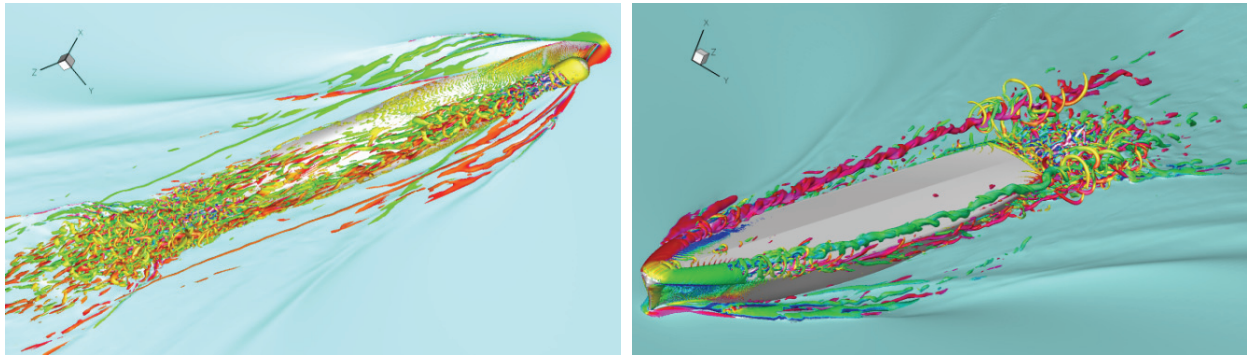


Fig. 19. Instantaneous vortical structures colored by streamwise vorticity for DTMB 5512 at $Fr = 0.41$. Left: water phase, $Q = 100$; Right: air phase, $Q = 500$.

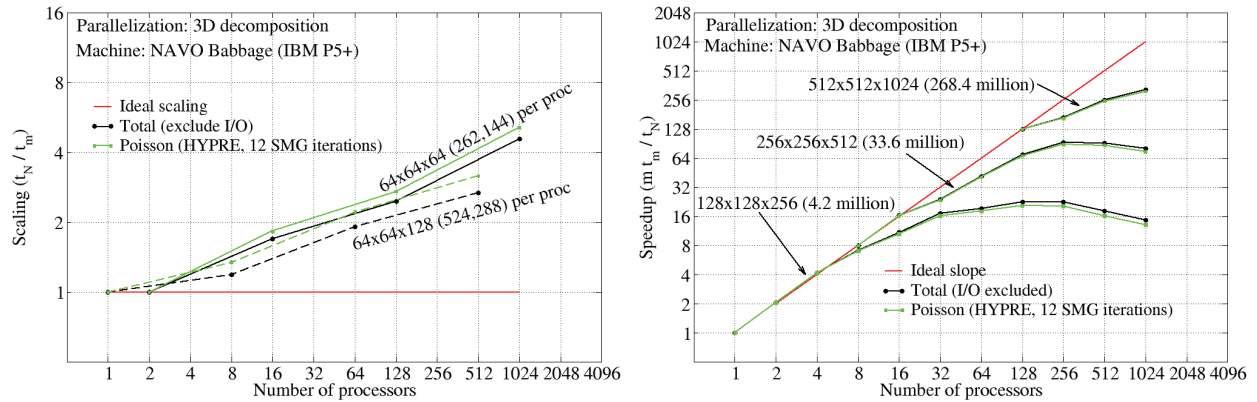


Fig. 20. Scalability of CFDShip-Iowa Version 6. Left: weak scalability; Right: strong scalability.